

Superconductivity in Pd-intercalated charge-density-wave rare earth poly-tellurides $R_E\text{Te}_n$

J. B. He^{†,‡}, P. P. Wang[†], H. X. Yang[†], Y. J. Long[‡], L. X. Zhao[‡], C. Ma[†], D. M. Wang[‡], X.
C. Shangguan[‡], Z. A. Ren[†], J. Q. Li[†], and G. F. Chen^{†,‡}

[†]Institute of Physics and Beijing National Laboratory for Condensed Matter Physics,
Chinese Academy of Sciences, Beijing 100190, China

[‡]Department of Physics, Renmin University of China, Beijing 100872, China

The interplay between magnetism and superconductivity is one of the dominant themes in the study of unconventional superconductors, such as high- T_c cuprates, iron pnictides and heavy fermions¹⁻³. In such systems, the same d - or f -electrons tend to form magnetically ordered states and participate in building up a high density of states at the Fermi level, which is responsible for the superconductivity. Charge-density-wave (CDW) is another fascinating collective quantum phenomenon in some low dimensional materials, like the prototypical transition-metal poly-chalcogenides, in which CDW instability is frequently found to accompany with superconducting transition at low temperatures⁴. Remarkably, similar to the antiferromagnetic superconductors, superconductivity can also be achieved upon suppression of CDW order via chemical doping or applied pressure in 1T-TiSe₂ (ref. 5, 6). However, in these CDW superconductors, the two ground states are believed to occur in different parts of Fermi surface (FS) sheets, derived mainly from chalcogen p -states and transition metal d -states, respectively. The origin of superconductivity and its interplay with CDW instability has not yet been unambiguously determined. Here we report on the discovery of bulk superconductivity in Pd-intercalated CDW $R_E\text{Te}_n$ (R_E =rare earth; $n=2.5, 3$) compounds, which belong to a large family of rare-earth poly-chalcogenides with CDW instability usually developing in the planar square nets of tellurium at remarkably high transition temperature and the electronic properties are also dominated by chalcogen p -orbitals. Our study demonstrates that the intercalation of palladium leads to the suppression of the CDW order and the emergence of the superconductivity. Our finding could provide an ideal model system for comprehensive studies of the interplay between CDW and superconductivity.

Charge density waves (CDWs) are periodic modulations of the conduction-electron-density in solids. They often present in low dimensional electronic systems^{4,7}. Usually, the CDW removes electrons from the Fermi level, and thus precludes a superconducting state⁸⁻¹⁰. However, in a variety of layered transition-metal dichalcogenides (TMDs), chain-type transition-metal trichalcogenides, and some organic compounds, CDW order coexists with superconductivity at low temperature^{4,7,11}. The interplay between the two correlated electronic states has become a topic of central interest in condensed matter physics¹²⁻¹⁴. Recently, superconductivity has also been found to arise upon suppression of CDW order in 1T-TiSe₂ via chemical doping⁵ or the application of pressure⁶. The CDW-superconductivity phase diagram is quite similar to those of heavy fermions, high- T_c cuprates and pnictides, in which the magnetic order is suppressed towards zero temperature through chemical doping or pressure¹⁻³. The superconductivity appears close to magnetic phase boundaries suggesting that magnetic fluctuations are responsible for the pairing mechanism¹⁵⁻¹⁷. However, in the case of 1T-TiSe₂, in spite of extensive theoretical and experimental efforts, the mechanism at the origin of the CDW and superconductivity is still unclear¹⁸⁻²³. It is particularly interesting to explore new systems with superconductivity closely proximity to the CDW instability, and to systematically study the interplay between CDW and superconductivity.

$R_E\text{Te}_n$ ($R_E=\text{Y, La-Sm, Gd-Tm}$; $n=2, 2.5, 3$), a large family of rare-earth poly-tellurides, has attracted much attention in recent years²⁴⁻³¹. Its particular interest lies in the correlation of the unique crystal structure with the charge-density wave formation. Remarkably, the rare earth tellurides show large anisotropic gap and very stable surface^{24, 25}, which provide us an exceptional opportunity to study CDW states using angle resolved photoemission spectroscopy (ARPES). $R_E\text{Te}_n$ takes a layered, weakly orthorhombic crystal structure, in which square-planar Te sheets are sandwiched by corrugated double layers of $R_E\text{Te}$ ^{26, 31}. $R_E\text{Te}_2$ contains a single layer of Te sheet, $R_E\text{Te}_3$ contains double layers of Te sheets connecting via Van der Waals force, while for $n=2.5$, i.e.

$R_{E2}Te_5$, the crystal structure can be viewed as alternatively stacking R_ETe_3 and R_ETe_2 slabs along the b-axis, which contains both single and double Te square sheets. The corrugated R_ETe -slab is insulating and responsible for magnetism in the case of magnetic rare earth ion R_E , while the square Te-layer forms a two-dimensional conduction band³¹⁻³⁴. It is very different from the case of layered TMD's, in which the triangular planes of transition metal ions dominate the electronic properties^{12,35}. In these rare earth poly-tellurides, the incommensurate/commensurate CDWs are also localized on the planar square nets of tellurium with a remarkably high transition temperature, as confirmed by the observation of superstructure above the room temperature^{28, 29, 36, 37}, where the CDW is demonstrated to be driven by the imperfect nesting of Fermi surfaces (FS)^{24, 33}. The observed metallic resistivity behavior in R_ETe_n ($n=2.5, 3$) confirmed further that the FS remains in a certain momentum region of the Brillouin zone even in the CDW state^{30, 32, 38}. The large anisotropy of the electrical conductivity demonstrates the strong two-dimensional nature due to the weak hybridization between the Te and the R_ETe layer^{30, 38}. Especially, $R_{E2}Te_5$ may represent a rare example to show a hybrid CDW distortion with two independent modulation vectors from two different Te nets^{28, 29}.

For R_ETe_3 and $R_{E2}Te_5$, due to the weak Van der Waals bonding between the adjacent square Te-sheets, the crystals have potential to allow interlayer insertion of guest metal atoms or organic molecules. In fact, a series of new compounds AMR_ETe_4 has been successfully synthesized by insertion of $AMTe$ layer in R_ETe_3 ($A=K, Na$; $M=Cu, Ag$; $R_E=La, Ce, Eu$)^{39, 40}. In this case, there is no electron transferring between the $[AMTe]$ and $[R_ETe_3]$ slabs. An evident change in the CDW character has been attributed to the alternation occurring in the interlayer coupling between adjacent Te nets of R_ETe_3 slabs upon insertion of the $AMTe$ layer^{41, 42}. In this work, we report the discovery of bulk superconductivity in R_ETe_n induced by Pd-intercalation (i.e., $Pd_xR_ETe_n$). The superconductivity is observed not only for the nonmagnetic rare earth elements Y, La, but also for the magnetic rare earths, Pr, Sm, Gd, Tb, Dy, Ho, Er, Tm, in which antiferromagnetism arising

from the local moments on the rare earth ions is found to coexist with superconductivity. In particular, we focus on two typical series, Pd_xHoTe_3 and $\text{Pd}_x\text{Y}_2\text{Te}_5$. For Pd_xHoTe_3 , with increasing the Pd content (x), the CDW transition is continuously suppressed, and the superconducting state appears at $x=0.04$. Within the range of solid solution, the superconducting transition temperature T_c has a dome-like shape in the doping-temperature phase diagram with a maximum near $x=0.08$ ($T_c=2.83$ K). The CDW-superconductivity phase diagram is quite similar to that of high- T_c cuprates or iron pnictides^{1,2}. For $\text{Pd}_x\text{Y}_2\text{Te}_5$, Pd-intercalation only occurs between the double layers of Te sheets, in which the CDW can be suppressed by continuous Pd doping, and superconductivity emerges with a maximum $T_c=3.05$ K ($x=0.08$). TEM results confirmed that Pd-intercalation have little effect on the CDW state located on single Te square sheets. To our knowledge, this is the first example of superconductivity in an intercalated “rare earth” telluride. Our finding demonstrates the potential for exploring new superconductors in other rare-earth poly-chalcogenides, a large family of CDW hosts in which the conduction band is also predominantly formed from chalcogen p -orbitals. Furthermore, $\text{Pd}_x\text{R}_E\text{Te}_n$ offers an excellent opportunity to study the CDW to superconductivity transition through an easily controllable chemical parameter. Due to the same p -electrons are responsible for both superconductivity and CDW, it is very important to verify whether the origin of superconductivity in this family is the same as for TMD, or if other mechanisms are involved. Such systematic studies are believed to provide further insights into their possible underlying mechanisms.

Polycrystalline samples of $\text{Pd}_x\text{R}_E\text{Te}_n$ ($0 \leq x \leq 0.3$) were synthesized by solid-state reaction method. First, stoichiometric amount of rare earth elements R_E (3N5), Te (5N), and Pd (3N) powders were sealed in thick walled quartz tube under vacuum. The quartz tube was heated to moderate temperature (500-700°C) slowly and held there for 50 hours, and then cooled to room temperature naturally. Second, the resulting product was reground, pressed into a pellet, sealed in an evacuated quartz tube and reheated for a further 50 hours. After repeating this process several

times, homogeneous samples were obtained. The X-ray diffraction (XRD) pattern of the resulting samples was taken on a PANalytical diffractometer using Cu K_α radiation at room temperature. Magnetization measurements were carried out in MPMS SQUID VSM (Quantum Design) with zero-field-cooled (ZFC) and/or field-cooled (FC) modes. Transport and heat capacity properties were measured in PPMS system (Quantum Design). Microstructure analysis and in situ Transmission electron microscopy (TEM) observations were performed on a Tecnai F20 transmission electron microscope, equipped with low-temperature holders.

Figure 1a shows the highly two-dimensional crystal structure of $R_E\text{Te}_n$ family ($R_E=\text{Y, La-Sm, Gd-Tm}$): double sheets of nearly square planar tellurium (Te) are separated by a corrugated R_E -Te slab. Figure 1b and 1c show the powder X-ray diffraction patterns of HoTe_3 and Y_2Te_5 and Pd-doped samples with formula $\text{Pd}_x\text{R}_E\text{Te}_n$ (where $n=2.5, 3$; $x=0-0.25$), which can be well indexed using orthorhombic crystal structure (NdTe_n -type) with the space group $Cmcm$ ³¹. Detailed analysis of the X-ray data demonstrates an evident increase of lattice constant b with the increase of Pd doping content (x), as shown in Fig. 1d, indicating successful intercalation of the Pd into the weakly bonded double Te layers.

Figure 2a shows the temperature dependent resistivity $\rho(T)$ measured for polycrystalline samples of Pd_xHoTe_3 . Consistent with previous work³⁸, the resistivity of HoTe_3 shows a clear, sharp jump at approximately 285 K, a broad maximum centered at about 260 K, and a good metallic behavior at low temperature. This feature has been attributed to the partial gapping of the Fermi surface at the CDW transition⁴³. On doping with increasing amounts of Pd, the anomaly becomes broader, reduces in size and moves to the lower temperature. The superconductivity emerges at $x=0.04$, while a less pronounced anomaly is still observed at around 120 K. The highest $T_c=2.83$ K is obtained at $x=0.08$, which can be seen clearly from an expanded plot of the temperature-dependent resistivity curve, as shown in Fig. 2b. T_c is found to drop slightly with further Pd-doping. Interestingly, $\rho(T)$ shows a semiconducting-like behavior before the

superconducting transition. A similar behavior has also been observed in Pd doped 1T-TiSe₂ with a limited doping range⁴⁴, in contrast to Cu doping of 1T-TiSe₂, where increasing Cu content continuously improve the metallicity⁵. Further investigation is certainly needed to clarify this point.

Figure 2c shows the temperature dependence of electrical resistivity $\rho(T)$ measured for polycrystalline samples of Pd_xY₂Te₅. One can see that, for pure Y₂Te₅, with decreasing temperature, $\rho(T)$ increases rapidly around 300 K, followed by a broad hump centered at about 200 K, and then decreases slowly. Such an anomaly observed in the family of rare earth tritellurides $R_E\text{Te}_3$ is associated with the CDW transition, but $R_E\text{Te}_3$ exhibits a good metallic behavior at low temperature⁴⁵. Actually, we cannot clarify the CDW transition upon the presented data. The appearance of the prominent broad peak in $\rho(T)$ for Y₂Te₅ seems to have another reason. Earlier studies have shown that, in $R_{E2}\text{Te}_5$, the single layer Te sheets are tellurium deficient, while the double Te sheets have essentially perfect square symmetry³⁰. So, in $R_{E2}\text{Te}_5$, the large resistivity and the broad maximum far below room temperature, might be described by a two-component scaling function composed of a semiconducting phase and metallic phase, as observed T -dependent resistivity in the family of $R_E\text{Te}_{2-8}$ and $R_E\text{Te}_3$ (ref. 32, 46). With Pd doping, the huge hump anomaly shifts to lower temperature and becomes less pronounced. The superconductivity emerges at $x=0.04$, and the highest $T_c=3.05$ K is obtained at $x=0.08$. At higher temperatures, for samples with $0 \leq x \leq 0.06$, $\rho(T)$ displays slightly metal-like behavior down to 200 K.

The bulk superconductivity in Pd-doped $R_E\text{Te}_n$ is confirmed by dc magnetic susceptibility, as shown in Fig. 3a and 3b. With increasing Pd content in Pd_xHoTe₃, and Pd_xY₂Te₅, both the superconducting transition temperature and the diamagnetic signal increase and reach the maximum at $x=0.08$; further increase in x results in suppression of the signal strength and T_c . The

shielding volume fraction at 1.8 K is estimated to be 100% for optimal doping sample. Specific heat C_p measurement carried out at $H=0$, and 1 T for $\text{Pd}_{0.08}\text{Y}_2\text{Te}_5$, is shown in Fig. 3c. The peak was suppressed with applied magnetic field, as expected for a superconducting transition. One can see that the specific jump near T_c is very sharp with $H=0$, indicating the good quality of the sample. Below 10 K, the normal state specific heat $C(T)$ can be well fitted by a relation, $C_p=\gamma T+\beta T^3$, indicating that the specific heat C_p is mainly contributed by electrons and phonons. The fit yields the electronic coefficient $\gamma=2\text{ mJ/molK}^2$, and the Debye temperature $\Theta_D=207\text{ K}$. Using the $\gamma=2\text{ mJ/molK}^2$ and $T_c=3\text{ K}$, we obtained $\Delta C_p/\gamma T_c=1.63$, slightly larger than the value of 1.43 within the BCS weak coupling approximation.

In Fig. 3d, we present the temperature dependence of magnetic susceptibility $\chi(T)$ for $\text{Pd}_{0.08}\text{HoTe}_3$ in the low temperature region with a magnetic field of 10 Oe. Near 3.5 K, χ tends to show a small peak, and followed by a clear diamagnetic drop corresponding to superconducting transition at around 2.8 K, which corresponds to the zero resistivity temperature. To get more information about the magnetic properties, we performed the dc magnetic susceptibility measured at the magnetic field of 0.1 T, as shown in the lower inset of Fig. 3d. Above 50 K, the data are well fitted with a simple Curie-Weiss law with an effective magnetic moment of $10.82\text{ }\mu_B$, which is close to the magnetic moment of free Ho^{3+} ion. The sharp drop below 3 K here is due to the AFM ordering, which is consistent with the specific heat data (the upper inset of Fig. 3d). All these results indicate that the superconductivity coexists with the AFM ordering of $R_E\ 4f$ local moments due to the weak exchange interaction between the local rare earth $4f$ moments and Te $5p$ conduction electrons. Similar phenomena has been reported in other systems, such as $R_E\text{Rh}_4\text{B}_4$, $R_E\text{Mo}_6\text{S}_8$, and $R_E\text{Ni}_2\text{B}_2\text{C}$, in which the crystallographic site for the magnetic ions (R_E ions) is well isolated from the conduction path⁴⁷⁻⁴⁹.

As discussed above, for $\text{Pd}_{0.08}\text{Y}_2\text{Te}_5$ without the rare earth $4f$ electrons, the superconducting transition is clearly observable at $T_c \sim 3$ K. On the contrary, there is no specific heat discontinuity surrounding T_c related to superconducting transition for $\text{Pd}_{0.08}\text{HoTe}_3$, as shown in the upper inset of Fig. 3d, due to the large background specific heat caused by both magnetic and crystal electric field (CEF) effects, which impedes the resolution of the superconducting jump⁴⁵. Similar behavior has also been seen for the typical magnetic superconductor $\text{HoNi}_2\text{B}_2\text{C}$ (ref. 50). In particular, in this case, the superconducting transition temperature is very close to the AFM order ($T_N/T_c < 1.2$), so it is not possible to extract the superconducting contribution from the strong background.

An important parameter to characterize superconductivity is the upper critical field $H_{c2}(0)$. We measured the temperature-dependent resistivity of the optimal doping samples, $\text{Pd}_{0.08}\text{HoTe}_3$, and $\text{Pd}_{0.08}\text{Y}_2\text{Te}_5$, under different magnetic fields, as shown in Fig. 4a and 4b. The corresponding upper critical field H_{c2} versus T_c is plotted in Fig. 4c and 4d, where T_c is defined by a criterion of 50% of normal state resistivity. One can see that, with increasing the magnetic field, the transition temperature T_c shifts to lower temperature and the transition width gradually becomes broader, similar to the high T_c iron-based superconductors², suggesting the strong anisotropy of the critical field, as expected from the two-dimensional electronic structure³³. The values of $-dH_{c2}/dT/T_c$ are -0.42 for $\text{Pd}_{0.08}\text{HoTe}_3$, and -0.62 for $\text{Pd}_{0.08}\text{Y}_2\text{Te}_5$, respectively. Using the Werthamer-Helfand-Hohenberg formula⁵¹, $H_{c2}(0) = -0.69(dH_{c2}/dT)T_c$, and taking $T_c = 2.8$ K, and 3 K, the upper critical fields are estimated to be 0.81 T and 1.28 T, respectively. Figure 4e and 4f depict the $M(H)$ versus H plot at 1.5-3 K measured by sweeping the magnetic field at a constant rate of 1 Oe/sec, which indicates that $\text{Pd}_x\text{R}_E\text{Te}_n$ is a type-II superconductor with a strong vortex pinning. The lower critical fields H_{c1} were estimated to be 15 Oe for $\text{Pd}_{0.08}\text{HoTe}_3$ and 20 Oe for $\text{Pd}_{0.08}\text{Y}_2\text{Te}_5$, respectively, which are smaller than that of the copper-intercalated 1T-TiSe_2 with $T_c = 4.15$ K (ref. 5).

Now let us take an overall view on the properties of other Pd-doped rare earth tritellurides. Figure 5 shows the low temperature dependent resistivity for $\text{Pd}_{0.08}R_E\text{Te}_3$ ($R_E=\text{La, Pr, Sm, Gd, Tb, Dy, Er}$ and Tm) samples. One can see that, for the heavy rare earth tritellurides with the element changing from Gd, Tb to Tm, all compounds exhibit superconductivity with $T_c \sim 2\text{-}3$ K, while for the light rare earth compounds $\text{Pd}_{0.08}\text{LaTe}_3$, $\text{Pd}_{0.08}\text{PrTe}_3$, $\text{Pd}_{0.08}\text{SmTe}_3$, they show superconductivity at relatively low temperatures ($T_c < 1$ K). At present stage, resistivity measurements for Pd-doped CeTe_3 and NdTe_3 samples do not show superconductivity with the temperature down to 50 mK. Several possible reasons for the suppression of superconductivity in light rare earth compounds are considered here. Firstly, the suppression of superconductivity might arise from the magnetic pair breaking effect. For example, in $R_E\text{Ni}_2\text{B}_2\text{C}$, the T_c changes from 16.6 K in $(\text{Lu, Y})\text{Ni}_2\text{B}_2\text{C}$ to 0 K for $\text{TbNi}_2\text{B}_2\text{C}$, in which the decrease of T_c is roughly scaled by de Gennes factor $DG = (g-1)^2 J(J+1)$, implying the dominance of the magnetic pair breaking effect in the systematic change of T_c with the rare earth element⁵². However, in our case, the T_c change between Pd_xTmTe_3 and Pd_xGdTe_3 is less than 1 K. Here the antiferromagnetism doesn't affect superconductivity dramatically regarding T_c , because the $4f$ moments due to the R_E sublattice is electronically isolated from the Te square nets, and hence no strong pair breaking occurs in the conducting square nets of Te. Secondly, the absence of superconductivity may be ascribed to the hybridization of the $4f$ electrons with itinerant conduction electrons. Among of them, CeTe_3 shows a moderate heavy fermion behavior, and the occurrence of spin density wave (SDW) at low temperature ($T_{SDW} = 1.3$ K) has been proposed according to the neutron diffraction and specific heat measurements⁵³. Recent ARPES result also shows that, in CeTe_3 , the $4f^d$ peak moves closer to the Fermi level (-0.28 eV), which is actually different from other $R_E\text{Te}_3$ materials⁴³.

Lastly, although the Fermi surface is composed of states associated with the double Te layers in $R_E\text{Te}_3$, the change of the rare-earth element has been found to cause a remarkable difference in the periodic lattice distortion (PLD) nesting vector, as well as the transport and magnetic

properties due to the effect of “chemical pressure”^{32,36,38}. For example, the CDW transition temperatures reduce obviously from the light to heavy rare-earth elements³⁸. A similar variation of the CDW properties could also be induced by applied pressure^{54,55}. In addition, recent ARPES results have pointed out that the percentage of ungapped FS changes from 35% in CeTe₃ to 55% in DyTe₃, giving a strong R_E dependence⁴⁰. The change of lattice spacing causes the changed electronic structure compared to the cases of R_E with small ionic radius, like Tm, in particular the reduced density of states at the Fermi level $N(E_F)$. We noticed that, for heavy rare earth tritellurides except for the Gd, Tb compounds, the second CDW transition T_{CDW2} formed at the low temperature has been observed clearly in the temperature dependent resistivity for these parent compounds³⁵. T_{CDW2} was found to decrease with the increasing of the lattice parameter, eventually vanishing for TbTe₃, which shows the opposite trend compared to the first CDW transition³⁵. It seems that there is some connection between the chemical pressure induced second CDW transition and superconductivity. But the effect of lattice structure alone is not sufficient to explain the suppression of superconductivity for light rare earth tri-tellurides, since Pd_xLaTe₃ superconducts at $T_c \sim 0.6$ K in spite of relatively large lattice constant ratio b/a . Therefore, it is reasonable to consider here that the suppression of superconductivity for light rare earth tellurides is ascribed to the combination of multiple effects.

Previous TEM and high resolution X-ray scattering measurements revealed that the rare-earth tritellurides $R_E\text{Te}_3$ compounds often incommensurate modulated structures arising from CDW, the modulation appears along c^* axis direction with their wave vectors ranging from $0.2719\ c^*$ to $0.3028\ c^*$ for $R_E = \text{La to Tm}$ ⁵⁶. Moreover, it has been also demonstrated that $R_{E2}\text{Te}_5$ compounds contain two sets of structural modulations corresponding with two different CDW states in the single and double Te planes, respectively^{29,54}; the visible modulation from the CDW state in the double Te planes adopts an incommensurate periodicity similar with what observed in $R_E\text{Te}_3$. On the other hand, the other modulations from a CDW state in the single Te planes have

the commensurate nature. TEM investigations in Gd_2Te_5 revealed the commensurate structural modulations can be written as $q_1 = 5/12a^* + 1/12c^*$ and $q_2 = 1/12a^* + 5/12c^*$ (ref. 57).

In order to reveal the structural features in correlation with the CDW transitions and superconductivity in the rare-earth poly-tellurides, we have carried out a number of in-situ TEM observations with a number of well-characterized samples. For the parent phases $R_E\text{Te}_3$ and $R_{E2}\text{Te}_5$, similar structural modulations and microstructure features for CDW states have been observed as reported in previous literatures^{26, 28, 57}. Moreover, our careful analysis suggests that the incommensurate modulation become evidently invisible in superconducting samples, this fact demonstrates that the CDW states formed in the double Te planes is efficiently suppressed in association with the appearances of superconductivity. Figures 6a and 6b show, respectively, the [010] zone-axis Selected Area Electron Diffraction (SAED) patterns taken at the temperature around 100 K for TmTe_3 and $\text{Pd}_{0.08}\text{TmTe}_3$. It is recognizable that notable incommensurate diffraction spots, as indicated in Fig. 6a, disappear completely in Fig. 6b which is obtained from a superconducting sample. Similar experimental results have been also obtained based on diffraction observations for the Y_2Te_5 CDW phase and $\text{Pd}_{0.08}\text{Y}_2\text{Te}_5$ superconducting phase, as clearly illustrated in the low-temperature SAED patterns of Fig.6c and 6d, respectively.

Figure 7 is the phase diagram showing the resistivity anomaly (open circles) and superconducting transition (closed circles) temperatures as a function of Pd content in Pd_xHoTe_3 . The T - x electronic phase diagram is quite similar to that of Cu_xTiSe_2 (ref. 5), where the superconductivity emerges when the CDW order is destroyed by doping. However, one should be noted that, an important difference between the two is that, for Cu-intercalated $1T\text{-TiSe}_2$, the doped electrons enter the bottom of the Ti $3d$ -induced conduction band, which dominates the electronic properties^{35, 58}, while the Pd atom has a $4d^{10}5s^0$ configuration, it seems that no electron transfer between Pd and $R_E\text{Te}_n$. Furthermore, the Fermi surface of $R_E\text{Te}_n$ is derived mainly from the p -orbitals of the Te atoms, which are formed the double layers of nearly square-planar sheets;

and the contribution near E_F from R_E $4f$ states is negligible³¹⁻³⁴. Further theoretical and spectroscopic studies will be helpful to understand the underlying mechanism.

In summary, we have synthesized series of materials $\text{Pd}_x\text{R}_E\text{Te}_n$ by solid-state reaction. The parent compounds, R_ETe_n , develop CDW instability with a moderately high transition temperature. It is found that the CDW order could be suppressed continuously by intercalation of Pd, and induces bulk superconductivity for a limit range of Pd concentrations. Such a phase diagram is reminiscent of that in the well studied copper-intercalated $1T\text{-TiSe}_2$, while the simplicity of the electronic structure of the Te planes in R_ETe_n makes it a good candidate to carry out a complete study of the relation between the CDW and superconductivity.

References

1. Bednorz, J. G. & Müller, K. A. Possible high T_c superconductivity in the Ba-La-Cu-O system. *Z. Phys. B* **64**, 189 (1986).
2. Chen, G. F. et al. Superconductivity at 41 K and its competition with spin-density-wave instability in layered $\text{CeO}_{1-x}\text{F}_x\text{FeAs}$. *Phys. Rev. Lett.* **100**, 247002 (2008).
3. Mathur, N. D. et al. Magnetically mediated superconductivity in heavy fermion compounds. *Nature* **394**, 39 (1998).
4. Grüner, G. The dynamics of charge-density waves. *Rev. Mod. Phys.* **60**, 1129 (1988).
5. Morosan, E. et al. Superconductivity in Cu_xTiSe_2 . *Nature Physics* **2**, 544 (2006).
6. Kusmartseva, A. F., Sipos, B., Berger, H., Forró L., & Tutiš, E. Pressure induced superconductivity in pristine 1T-TiSe₂. *Phys. Rev. Lett.* **103**, 236401 (2009).
7. Grüner, G. *Density Waves in Solids* (Addison-Wesley, Reading, MA, 1994).
8. Levin, K., Mills, D. L & Cunningham, S. L. Incompatibility of BCS pairing and the Peierls distortion in one-dimensional systems. I. mean-field theory. *Phys. Rev. B* **10**, 3821 (1974).
9. Balseiro, C. A. and Falicov, L. M. Superconductivity and charge-density waves. *Phys. Rev. B* **20**, 4457 (1979).
10. Milán del Bosch, L. & Yndurán, F. Coexistence of spiral spin-density waves and superconductivity: ground-state properties. *Phys. Rev. B* **41**, 2540 (1990).
11. Ishiguro T., Yamaji K., Saito G., *Organic Superconductors* (Springer-Verlag, Berlin, Heidelberg 1998).

12. Yokoya, T. et al. Fermi surface sheet-dependent superconductivity in $2H\text{-NbSe}_2$. *Science* **294**, 2518 (2001).
13. Kiss, T. et al. Charge-order-maximized momentum-dependent superconductivity. *Nature Physics* **3**, 720 (2007).
14. Fainchtein, R., D'Arcangelis, S. T., Yang, S. S. & Cowan, D. O. Order and low dimensionality in the organic superconductor $(\text{BEDT-TTF})_2\text{Cu}(\text{NCS})_2$ revealed by STM. *Science* **256**, 1012 (1992).
15. Hayden, S. M., Mook, H. A., Dai, P., Perring, T. G. & Doğan, F. The structure of the high-energy spin excitations in a high-transition-temperature superconductor. *Nature* **429**, 531 (2004).
16. de la Cruz, C. et al. Magnetic order close to superconductivity in the iron-based layered $\text{LaO}_{1-x}\text{F}_x\text{FeAs}$ systems. *Nature* **453**, 899 (2008).
17. Gegenwart, P., Si, Q. & Steglich, F. Quantum criticality in heavy-fermion metals. *Nature Physics* **4**, 186 (2008).
18. Zunger, A. & Freeman, A. J. Band structure and lattice instability of TiSe_2 . *Phys. Rev. B* **17**, 1839 (1978).
19. Monney, C. et al. Spontaneous exciton condensation in $1T\text{-TiSe}_2$: BCS-like approach. *Phys. Rev. B* **79**, 045116 (2009).
20. Monney, C., Battaglia, C., Cercellier, H., Aebi, P. & Beck, H. Exciton condensation driving the periodic lattice distortion of $1T\text{-TiSe}_2$. *Phys. Rev. Lett.* **106**, 106404 (2011).

21. Cercellier, H. et al. Evidence for an excitonic insulator phase in 1T-TiSe₂. *Phys. Rev. Lett.* **99**, 146403 (2007).
22. Li, G. et al. Semimetal-to-semimetal charge density wave transition in 1T-TiSe₂. *Phys. Rev. Lett.* **99**, 027404 (2007).
23. Barath, H. et al. Quantum and classical mode softening near the charge-density-wave-superconductor transition of Cu_xTiSe₂. *Phys. Rev. Lett.* **100**, 106402 (2008).
24. Gweon, G. -H. et al. Direct observation of complete Fermi surface, imperfect nesting, and gap anisotropy in the high-temperature incommensurate charge-density-wave compound SmTe₃. *Phys. Rev. Lett.* **81**, 886 (1998).
25. Schmitt, F. et al. Transient electronic structure and melting of a charge density wave in TbTe₃. *Science* **321**, 1649 (2008).
26. Malliakas, C., Billinge, S. J. L., Kim, H. J., & Kanatzidis, M. G. Square nets of tellurium: rare-earth dependent variation in the charge-density wave of R_ETe₃ (RE = rare-earth element). *J. Am. Chem. Soc.* **127**, 6510 (2005).
27. Yao, H., Robertson, J. A., Kim, E., & Kivelson, S. A. Theory of stripes in quasi-two-dimensional rare-earth tellurides. *Phys. Rev. B* **74**, 245126 (2006).
28. Shin, K. Y. et al. Charge density wave formation in R₂Te₅ (R=Nd, Sm, and Gd). *Phys. Rev. B* **77**, 165101 (2008).
29. Malliakas, C. D., Iavarone, M., Fedor, J., & Kanatzidis, M. G. Coexistence and coupling of two distinct charge density waves in Sm₂Te₅. *J. Am. Chem. Soc.* **130**, 3310 (2008).

30. Pfunder, F., Degiorgi, L., Shin, K. Y. & Fisher, I. R. Optical properties of the charge-density-wave polychalcogenide compounds $R_2\text{Te}_5$ ($R=\text{Nd}$, Sm and Gd). *Eur. Phys. J. B* **63**, 11 (2008).
31. DiMasi, E., Foran, B., Aronson, M. C., & Lee, S. Quasi-two-dimensional metallic character of Sm_2Te_5 and SmTe_3 . *Chem. Mater.* **6**, 1867 (1994).
32. Iyeiri, Y., Okumura, T., Michioka, C., & Suzuki, K. Magnetic properties of rare-earth metal tritellurides $R\text{Te}_3$ ($R = \text{Ce}$, Pr , Nd , Gd , Dy). *Phys. Rev. B* **67**, 144417 (2003).
33. Brouet, V. et al. Fermi surface reconstruction in the CDW state of CeTe_3 observed by photoemission. *Phys. Rev. Lett.* **93**, 126405 (2004).
34. Laverock, J. et al. Fermi surface nesting and charge-density wave formation in rare-earth tritellurides. *Phys. Rev. B* **71**, 085114 (2005).
35. Qian D. et al. Emergence of Fermi pockets in a new excitonic charge-density-wave melted superconductor. *Phys. Rev. Lett.* **98**, 117007 (2007).
36. DiMasi, E., Aronson, M. C., Mansfield, J. F., Foran, B. & Lee, S. Chemical pressure and charge-density waves in rare-earth tritellurides. *Phys. Rev. B* **52**, 14516 (1995).
37. Shin, K. Y., Brouet, V., Ru, N., Shen, Z. X., & Fisher, I. R. Electronic structure and charge-density wave formation in $\text{LaTe}_{1.95}$ and $\text{CeTe}_{2.00}$. *Phys. Rev. B* **72**, 085132 (2005).
38. Ru, N. et al. Effect of chemical pressure on the charge density wave transition in rare-earth tritellurides $R\text{Te}_3$. *Phys. Rev. B* **77**, 035114 (2008).

39. Patschke, R., Heising, J., Kanatzidis, M., Brazis, P. & Kannewurf C. R. KCuCeTe₄: a new intergrowth rare earth telluride with an incommensurate superstructure associated with a distorted square net of tellurium. *Chem. Mater.* **10**, 695 (1998).
40. Patschke, R., Brazis, P., Kannewurf, C. R. & Kanatzidis, M. G. Cu_{0.66}EuTe₂, KCu₂EuTe₄ and Na_{0.2}Ag_{2.8}EuTe₄: compounds with modulated square Te nets. *J. Mater. Chem.* **9**, 2293 (1999).
41. Malliakas, C. D. & Kanatzidis, M. G. Charge density waves in the square nets of tellurium of AMR_ETe₄ (A = K, Na; M = Cu, Ag; R_E = La, Ce). *J. Am. Chem. Soc.* **129**, 10675 (2007).
42. Patschke, R. & Kanatzidis, M. G. Polytelluride compounds containing distorted nets of tellurium. *Phys. Chem. Chem. Phys.* **4**, 3266 (2002).
43. Brouet, V. et al. Angle-resolved photoemission study of the evolution of band structure and charge density wave properties in RTe₃ (R=Y, La, Ce, Sm, Gd, Tb, and Dy). *Phys. Rev. B* **77**, 235104 (2008).
44. Morosan, E. et al. Multiple electronic transitions and superconductivity in Pd_xTiSe₂. *Phys. Rev. B* **81**, 094524 (2010).
45. Ru, N., Chu, J. H., & Fisher, I. R. Magnetic properties of the charge density wave compounds RTe₃ (R=Y, La, Ce, Pr, Nd, Sm, Gd, Tb, Dy, Ho, Er, and Tm). *Phys. Rev. B* **78**, 012410 (2008).
46. Kwon, Y. S. & Min, B. H. Anisotropic transport properties in RTe₂ (R: La, Ce, Pr, Sm and Gd). *Physica B* **281&282**, 120(2000).
47. Fertig, W. A., Johnston, D. C., DeLong, L. E., McCallum R. W. & Maple, M. B. Destruction of superconductivity at the onset of long-range magnetic order in the compound ErRh₄B₄. *Phys. Rev. Lett.* **38**, 987 (1977).

48. Ishikawa, M. & Fischer, Ø. Destruction of superconductivity by magnetic ordering in $\text{Ho}_{1.2}\text{Mo}_6\text{S}_8$. *Solid State Commun.* **23**, 37 (1977).
49. Cava, R. J. et al. Superconductivity in the quaternary intermetallic compounds $\text{LnNi}_2\text{B}_2\text{C}$. *Nature* **367**, 252 (1994).
50. Park, T. & Salamon, M. B. Specific heat study of the magnetic superconductor $\text{HoNi}_2\text{B}_2\text{C}$. *Phys. Rev. B* **69**, 054505 (2004).
51. Werthamer, N. R., Helfand, E. & Hohenberg, P. C. Temperature and purity dependence of the superconducting critical field, H_{c2} . III. electron spin and spin-orbit effects. *Phys. Rev.* **147**, 295 (1966).
52. Eisaki, H. et al. Competition between magnetism and superconductivity in rare-earth nickel boride carbides. *Phys. Rev. B* **50**, 6470 (1994).
53. G. F. Chen, N. K. Sato., et al, unpublished.
54. Sacchetti, A. et al. Pressure dependence of the charge-density-wave gap in rare-earth tritellurides. *Phys. Rev. Lett.* **98**, 026401 (2007).
55. Hamlin, J. J. et al. Pressure-induced superconducting phase in the charge-density-wave compound terbium tritelluride. *Phys. Rev. Lett.* **102**, 177002 (2009).
56. Malliakas, C. D. and Kanatzidis, M. G., Divergence in the Behavior of the Charge Density Wave in $R_E\text{Te}_3$ (R_E =Rare-Earth Element) with Temperature and R_E Element. *J. Am. Chem. Soc.* **128**, 12612 (2006).
57. Shin, K.Y. et al. Observation of two separate charge density wave transitions in Gd_2Te_5 via transmission electron microscopy and high-resolution X-ray diffraction. *J. Alloy. Compd.* **489**, 332 (2010).

58. Jeong, T. & Jarlborg, T. Varying Cu-Ti hybridization near the Fermi energy in Cu_xTiSe_2 : results from supercell calculations. *Phys. Rev. B* **76**, 153103 (2007).

Acknowledgements

This work was supported by the Natural Science Foundation of China, and by the Ministry of Science and Technology of China.

Figure Legends

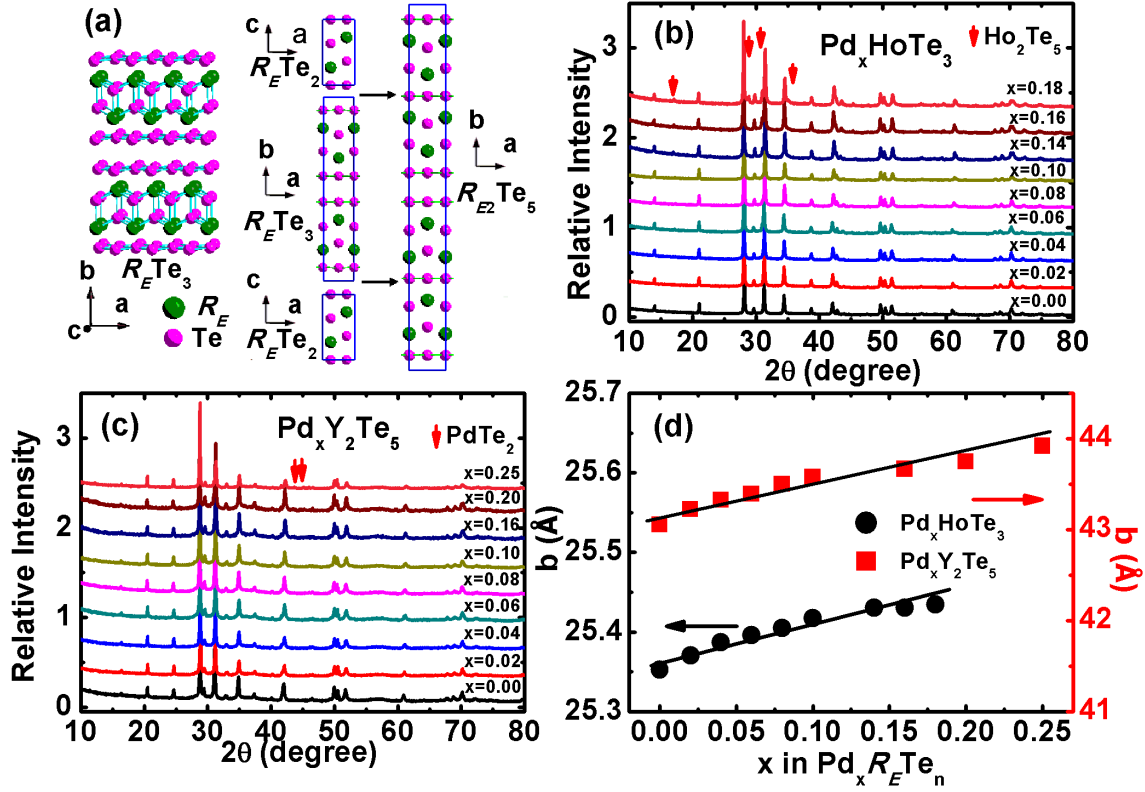


Figure 1. Crystal structural analyses of Pd_xHoTe_3 and $\text{Pd}_x\text{Y}_2\text{Te}_5$. **a**, Schematic crystal structures of $R_E\text{Te}_2$, $R_E\text{Te}_3$ and $R_{E2}\text{Te}_5$. The green and pink circles represent rare earth R_E and Te ions, respectively. Note that the $R_E\text{Te}$ -slab and Te-sheet are stacked along the b-axis. Pd ions are considered to be intercalated into the Van der Waals layer between double Te-sheets. **b**, **c**, Powder X-ray diffraction data collected for Pd_xHoTe_3 and $\text{Pd}_x\text{Y}_2\text{Te}_5$ with different Pd content. Impurity phases, as marked by the red arrows, appear only for samples with high doping level. **d**, Lattice parameter b as a function of x in Pd_xHoTe_3 and $\text{Pd}_x\text{Y}_2\text{Te}_5$. The straight line guides the eyes.

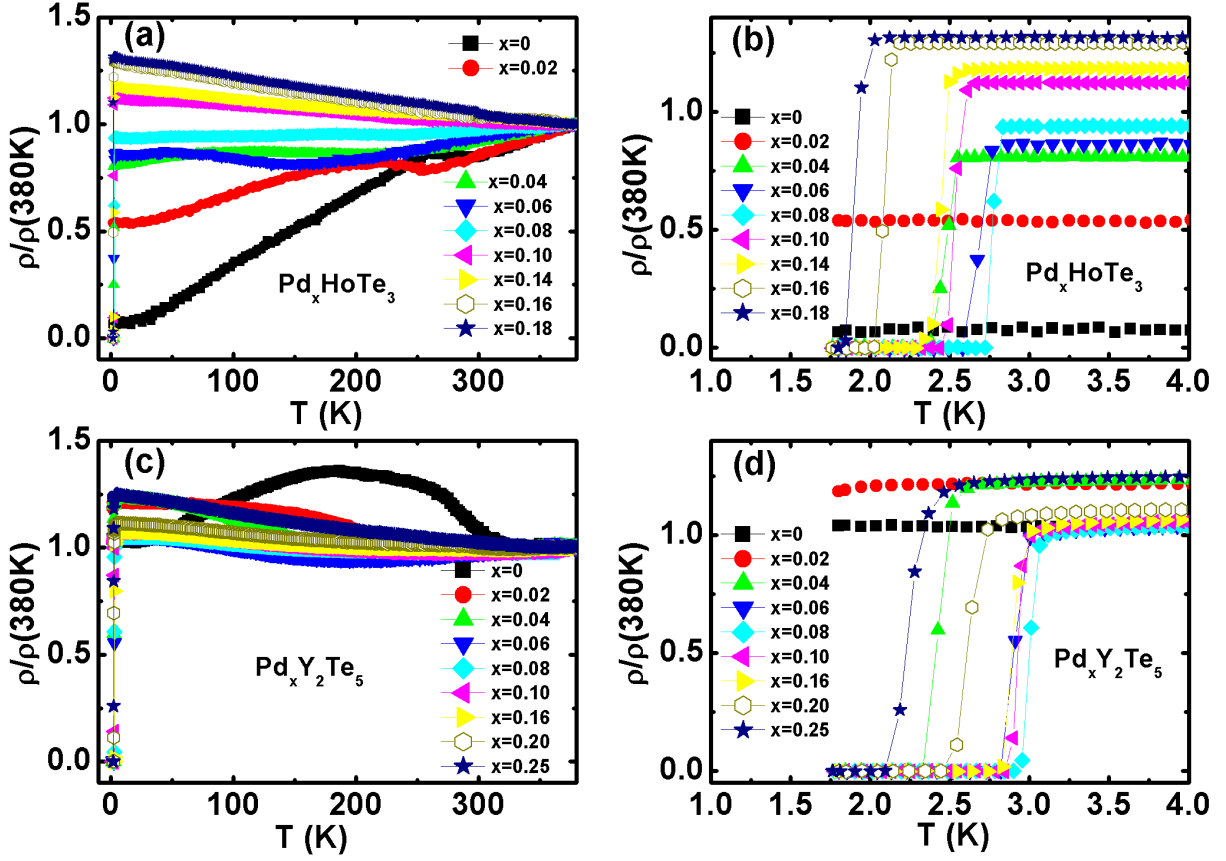


Figure 2. Transport properties of Pd_xHoTe_3 and $\text{Pd}_x\text{Y}_2\text{Te}_5$ with different Pd content. a, c, Normalized temperature dependent resistivity data measured on Pd_xHoTe_3 ($0 \leq x \leq 0.18$) and $\text{Pd}_x\text{Y}_2\text{Te}_5$ ($0 \leq x \leq 0.25$), respectively. With increasing x , the hump is suppressed and superconductivity emerges. b, d, T -dependent resistivity in an expanded region for Pd_xHoTe_3 and $\text{Pd}_x\text{Y}_2\text{Te}_5$ with different Pd content. Superconductivity appears for $x=0.04$, and T_c reaches a maximum for $x=0.08$. Further increasing Pd content, T_c is slowly suppressed.

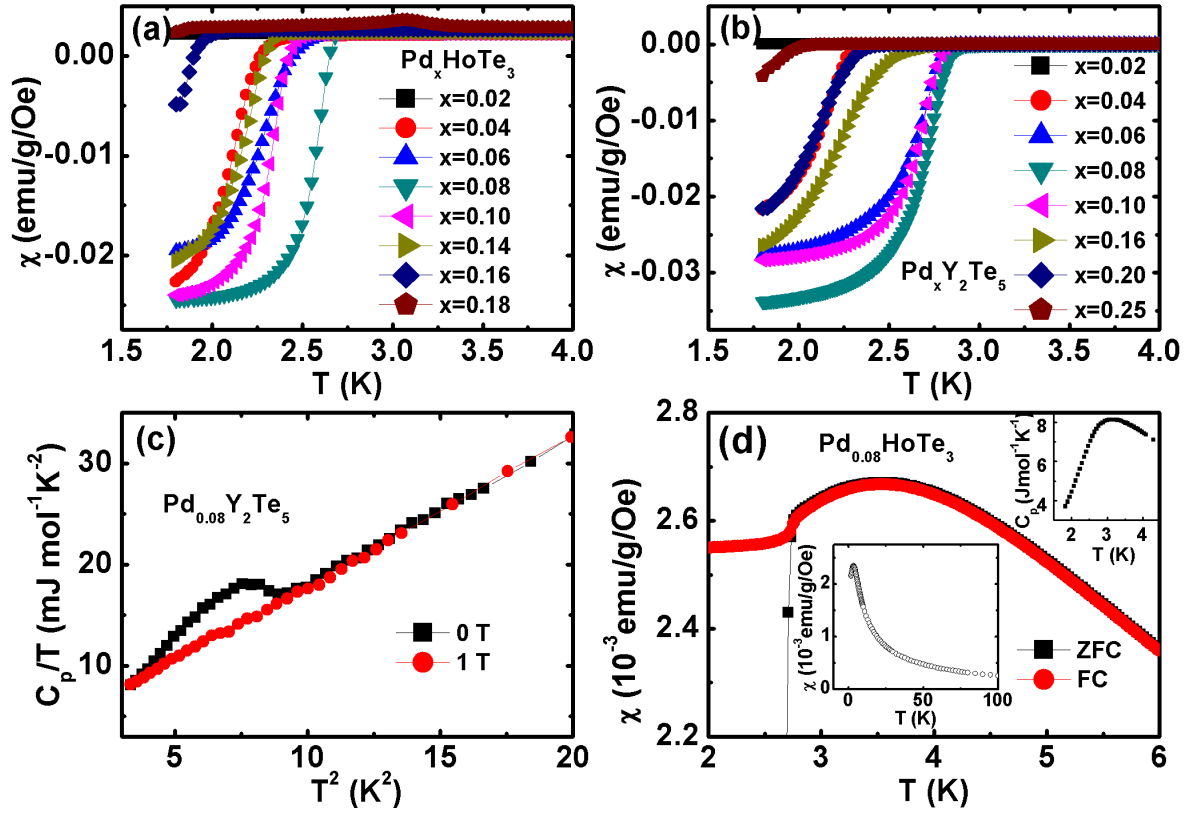


Figure 3. Characterization of the superconducting phase transitions for Pd_xHoTe_3 and $\text{Pd}_x\text{Y}_2\text{Te}_5$ with different Pd content. **a**, Low temperature magnetic susceptibility $\chi(T)$ for Pd_xHoTe_3 with $x = 0.02-0.18$. Data was collected in zero field cooled (ZFC) mode. **b**, $\chi(T)$ vs. T for $\text{Pd}_x\text{Y}_2\text{Te}_5$ with $x = 0.02-0.25$. **c**, The plot of C/T vs. T for the optimal doping sample $\text{Pd}_{0.08}\text{Y}_2\text{Te}_5$ at $H=0$ and 1 T. **d**, $\chi(T)$ vs. T for $\text{Pd}_{0.08}\text{HoTe}_3$ in the low temperature region with a magnetic field of 10 Oe. Upper inset: Heat capacity C_p vs. T for $\text{Pd}_{0.08}\text{HoTe}_3$. Lower inset: Temperature dependence of magnetic susceptibility $\chi(T)$ for $\text{Pd}_{0.08}\text{HoTe}_3$ measured with $H=0.1$ T.

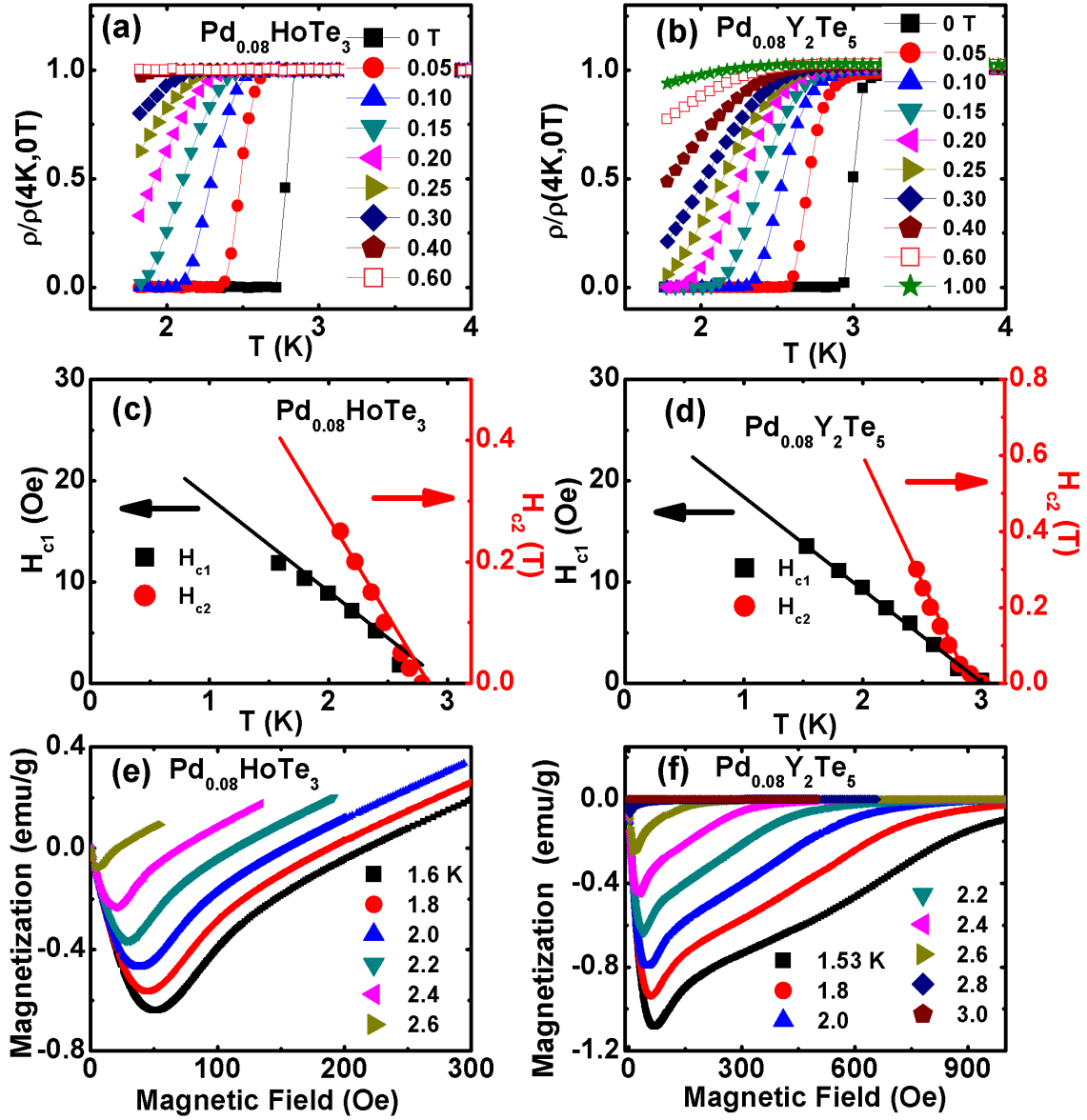


Figure 4. Characterization of the superconductivity state in $\text{Pd}_{0.08}\text{HoTe}_3$ and $\text{Pd}_{0.08}\text{Y}_2\text{Te}_5$. a, b, Temperature dependence of electrical resistivity for optimal doped $\text{Pd}_{0.08}\text{HoTe}_3$ and $\text{Pd}_{0.08}\text{Y}_2\text{Te}_5$ under various magnetic fields. c, d, H_c - T phase diagram, H_{c1} and H_{c2} , determined from $M(H)$ and $\rho(H)$ data. e, f, M versus H plots for selected temperatures at low magnetic fields.

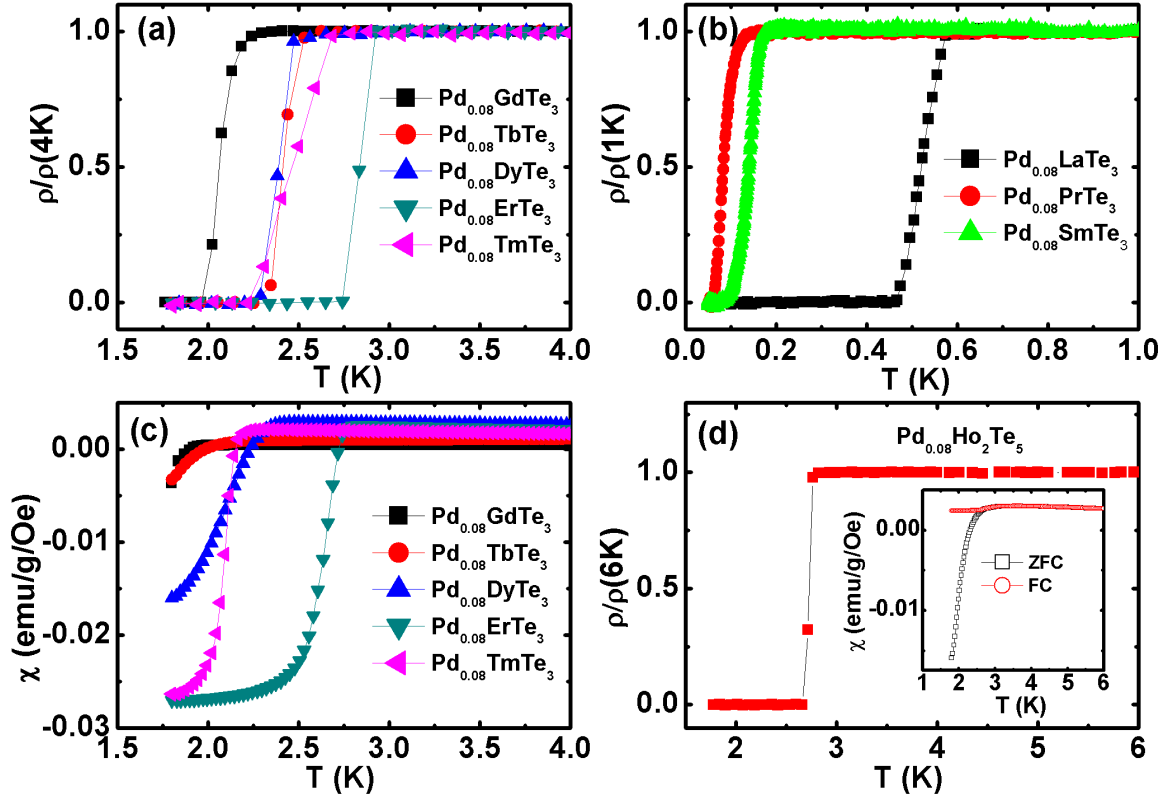


Figure 5. Characterization of the superconductivity transitions for $\text{Pd}_{0.08}\text{RETe}_3$. **a**, Normalized temperature dependent resistivity for heavy rare earth tri-tellurides $\text{Pd}_{0.08}\text{GdTe}_3$, $\text{Pd}_{0.08}\text{TbTe}_3$, $\text{Pd}_{0.08}\text{DyTe}_3$, $\text{Pd}_{0.08}\text{ErTe}_3$, and $\text{Pd}_{0.08}\text{TmTe}_3$. The critical temperatures T_c are 2.3, 2.55, 2.5, 2.9, 2.7 K, respectively. **b**, Low temperature resistivity data for light rare earth tri-tellurides $\text{Pd}_{0.08}\text{LaTe}_3$, $\text{Pd}_{0.08}\text{PrTe}_3$, and $\text{Pd}_{0.08}\text{SmTe}_3$, which superconduct at 0.6, 0.13, and 0.19 K, respectively. **c**, Temperature dependent dc magnetization in heavy rare earth tri-tellurides (Gd-Tm). **d**, Temperature dependent resistivity and dc magnetization for $\text{Pd}_{0.08}\text{Ho}_2\text{Te}_5$ ($T_c=2.8\text{ K}$).

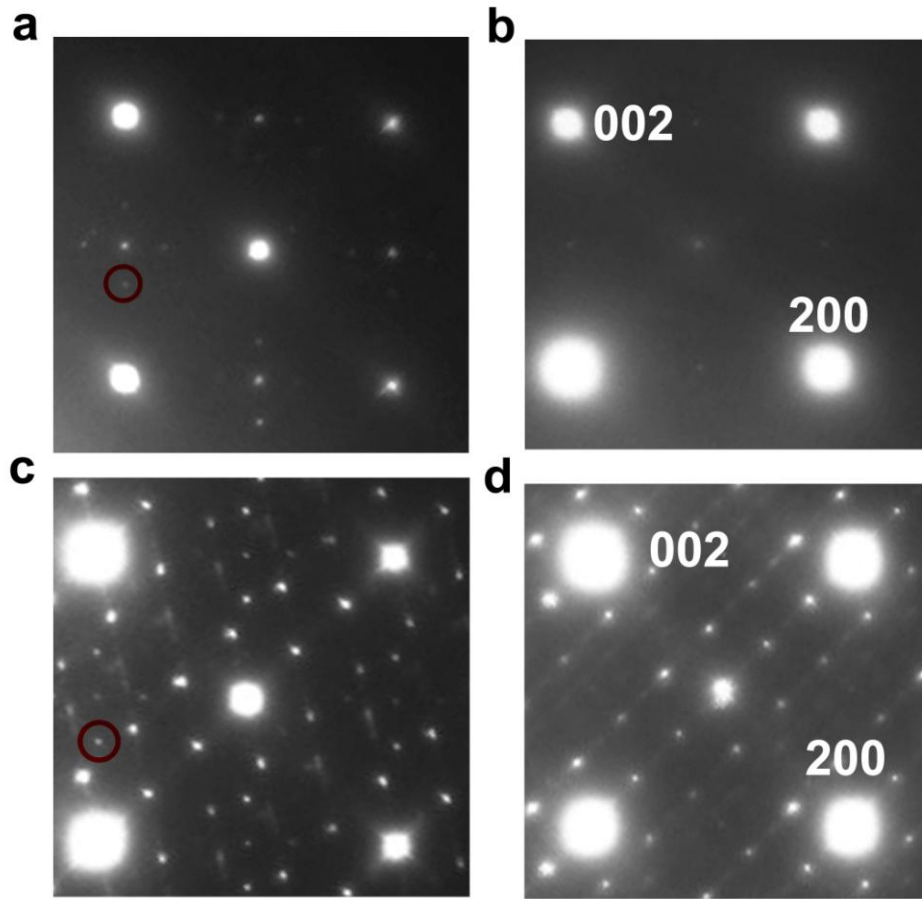


Figure 6 Structural modulations in parent CDW phases and superconducting phases. Electron diffraction patterns taken along the [010] zone-axis direction obtained at about 100 K. (a) TmTe₃, (c) Y₂Te₅ and (b) Pd_{0.08}TmTe₃, (d) Pd_{0.08}Y₂Te₅. Structural modulation from incommensurate CDW wave in the double Te planes can be clearly seen in the parent phases as indicated by circles.

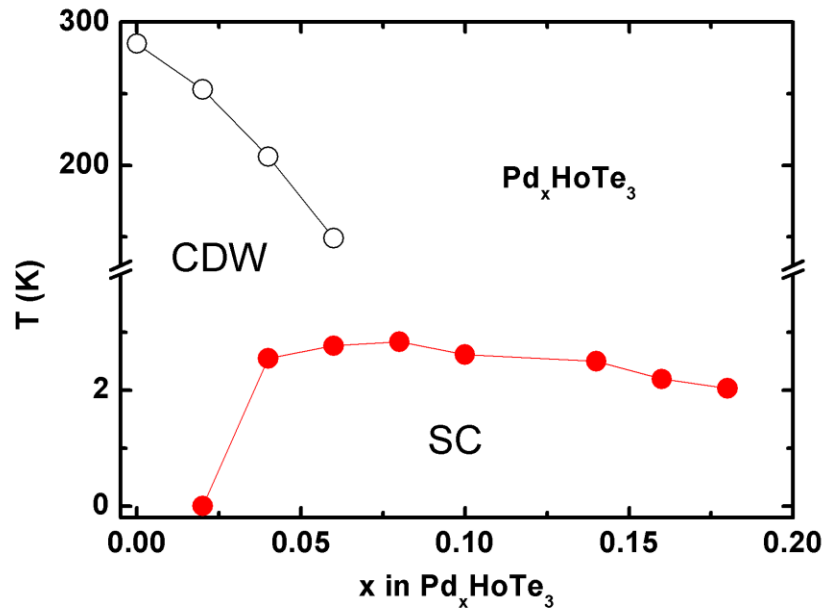


Figure 7. Electronic phase diagram for Pd_xHoTe_3 . Open and closed circles are determined from resistivity, which correspond to the first CDW transition temperature and superconducting transition temperature, respectively.